

Minimizing betatron coupling of energy spread and divergence in laser-wakefield accelerated electron beams

A. Koehler^{1,2,*}, R. Pausch¹, J.P. Couperus Cabadağ¹, O. Zarini^{1,2},
J.M. Krämer¹, M. Bussmann¹, A. Debus¹, U. Schramm^{1,2}, A. Irman¹

**1 Helmholtz-Zentrum Dresden - Rossendorf, Bautzner Landstrasse
400, 01328 Dresden, Germany**

2 Technische Universität Dresden, 01062 Dresden, Germany

* a.koehler@hzdr.de

Abstract

Matched beam loading in laser wakefield acceleration (LWFA), characterizing the state of flattening of the acceleration electric field along the bunch, leads to the minimization of energy spread at high bunch charges. Here, we demonstrate by independently controlling injected charge and acceleration gradients, using the self-truncated ionization injection scheme, that minimal energy spread coincides with a reduction of the normalized beam divergence. With the simultaneous confirmation of a constant beam radius at the plasma exit, deduced from betatron radiation spectroscopy, we attribute this effect to the reduction of chromatic betatron decoherence. Thus, beam loaded LWFA enables highest longitudinal and transverse phase space densities.

The concept of laser wakefield acceleration (LWFA) exploits the ultra-high accelerating field gradients of up to a few hundred gigavolt-per-meter generated in the wake of a high-intensity laser pulse as it propagates through an optically transparent plasma [1, 2]. Electron bunches can thus be accelerated to GeV energies within acceleration distances of only centimeters [3]. Beam quality with respect to bunch charge, energy bandwidth, emittance and pulse-to-pulse stability has improved substantially in the last decade and is closely linked to a variety of controlled electron injection techniques [4, 5, 6, 7, 8, 9]. Only recently it was demonstrated that laser plasma accelerators can be tailored for minimum energy spread at highest bunch charges by reshaping the local accelerating field by matched beam loading [10, 9]. This combination of high charge, essential in the beam loading regime, and the short bunch duration in the range of 10 fs [11, 12, 13, 14] result in high peak-currents exceeding 10 kA. Future applications, such as high-field THz sources [15], laboratory-size beam-driven plasma accelerators [16, 17, 18] and compact free-electron lasers [19, 20, 21, 22, 23], will require such compact and further improved high-brightness electron sources.

For taking full advantage of such high peak currents, not only the beam energy spread has to be minimized, but also divergence and thus beam emittance [24, 25]. In this letter, we address this point by showing how beam decoherence, schematically illustrated in Fig. 1, affects the transverse beam quality.

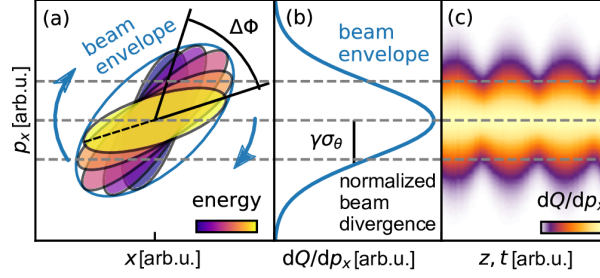


Figure 1. Beam decoherence: (a) illustrates the transverse phase space of a bunch with a finite energy spread consisting of many slices of different electron energy which rotate in phase space. The beam envelope encircles the sum of all slices. (b) shows the projection dQ/dp_x of the beam on p_x , which is typically recorded in experiments and used for measuring the beam divergence. (c) shows the time-dependence that is caused by the phase space rotation of the beam envelope. When the slices in (a) span over $\Delta\phi > \pi$, full decoherence is reached and the modulations in (c) vanish.

In transverse phase space (x, p_x) a polychromatic bunch can be divided into slices representing different energy classes. These then rotate with different angular frequencies according to the energy-dependent transverse focusing [26, 27]. A phase difference $\Delta\phi > \pi$ leads to full decoherence and thus the maximum in occupied phase space area, i.e. in beam divergence and size. Here, we demonstrate that beam loading besides minimizing the final energy spread also decreases the beam divergence by about 20%. Betatron radiation spectroscopy simultaneously confirms a constant beam radius of less than $1\ \mu\text{m}$ at the plasma exit. The small beam size and the minimized divergence improve the transverse beam quality and thus beam emittance, facilitating beam transport and novel applications.

At the matched beam loading condition, a balance between the bunch's self-fields and the acceleration field of the wakefield is reached, resulting in a constant longitudinal acceleration field along the bunch [28, 29], illustrated in Fig. 4(c) presenting simulation results discussed later in the text. All electrons within the bunch thus experience the same acceleration field so that no energy spread is added during the process. Besides acceleration, the wakefield provides strong linear focusing forces [30]. Off-axis electrons perform transverse (betatron) oscillations around the beam axis and emit betatron radiation while being accelerated [31, 32, 33, 34, 2]. Frequency, amplitude, and phase of the betatron motion strongly depend on the energy of electrons and their initial off-axis positions. At the end of the plasma accelerator, the motion of electrons in (x, p_x) defines the final beam size and transverse momentum distribution. Betatron radiation enables unique access to the micron-scale beam size at the plasma exit [35, 33, 36]. Bunches with finite energy spread experience decoherence of the betatron oscillations. As a consequence the envelope of a polychromatic beam performs significant oscillations [26, 27]. The beam loading condition can be effectively used to control beam decoherence, and thus the final beam emittance.

Experiments were performed with the DRACO Ti:Sapphire laser system [37]

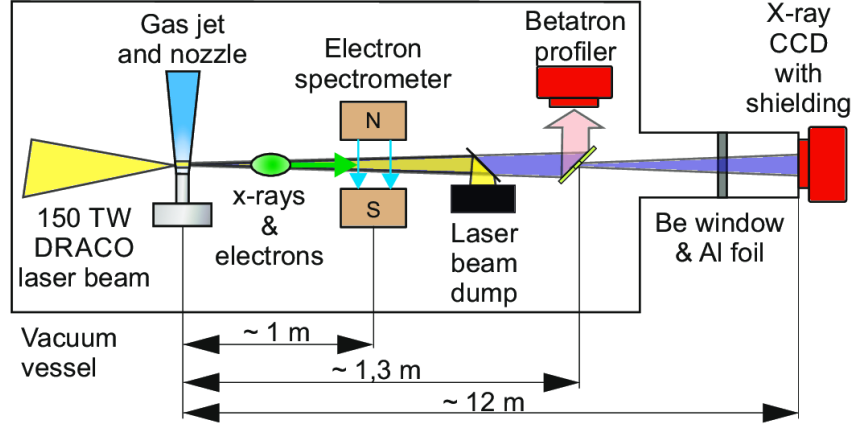


Figure 2. Experimental setup: The laser is focused on a gas jet and drives a wakefield. Accelerated electrons are energy analyzed in a magnet spectrometer. An aluminum foil blocks residual laser light behind the spectrometer. The scintillator of the betatron profiler intercepts the angular profile of the betatron radiation. On-axis betatron radiation passes through a hole of the profiler and is detected by the x-ray camera, which is separated from the interaction chamber by a beryllium window. An aluminum filter foil attenuates the betatron flux.

at the Helmholtz-Zentrum Dresden – Rossendorf. Fig. 2 shows a schematic of the setup. Laser pulses of 30 fs full-width at half-maximum (FWHM) duration with 2.5 J energy on target were focused with an off-axis parabolic mirror ($f/20$) to a vacuum focal spot size of $20\ \mu\text{m}$ (FWHM) yielding a normalized laser intensity of $a_0 \simeq 2.6$. The Strehl ratio of the wavefront-corrected beam was measured to be 0.9 by the laser energy within the beam waist (e^{-2} of intensity). The laser beam was focused $\sim 1.5\ \text{mm}$ beyond the entry of a 3 mm long de Laval gas nozzle [38]. The nozzle was operated with He-N₂ gas mixtures containing 0.2 % to 1.5 % of N₂. The gas density profile at 1.5 mm above the nozzle exit, i.e., the laser beam axis, was characterized by a dedicated interferometry setup [38] and consists of a 1.6 mm flat top region. Electrons were injected into the wakefield using self-truncated ionization injection (STII) [10, 39, 40], which enabled stable and reproducible shots with high charges of up to 500 pC (within FWHM) required for entering the beam loading regime. In order to measure the energy distribution, a 40 cm long permanent magnet dipole dispersed accelerated electrons to a set of charge calibrated scintillator screens (Konica Minolta OG 400) [41] that was read-out by charge coupled device (CCD) cameras.

A back-illuminated, deep depletion x-ray CCD (Princeton Instruments Pixis-XO 400BR) with $1340\ \text{pixel} \times 400\ \text{pixel}$ recorded betatron radiation emitted from the LWFA process. The camera was placed inside a dedicated radiation shielded area 12 m downstream of the plasma target, covering a solid angle of $1.5\ \text{mrad} \times 0.8\ \text{mrad}$. A $76\ \mu\text{m}$ thick beryllium window sealed the CCD chip, allowing for cooling and background noise reduction. An aluminum filter foil of $200\ \mu\text{m}$ thickness attenuated the betatron flux and enabled single-shot reconstruction of the betatron spectrum by counting single-photon absorption events [42, 36, 43]. Behind the electron spectrometer, a scintillator screen oriented at 45° with respect to the beam axis recorded the angle-resolved betatron

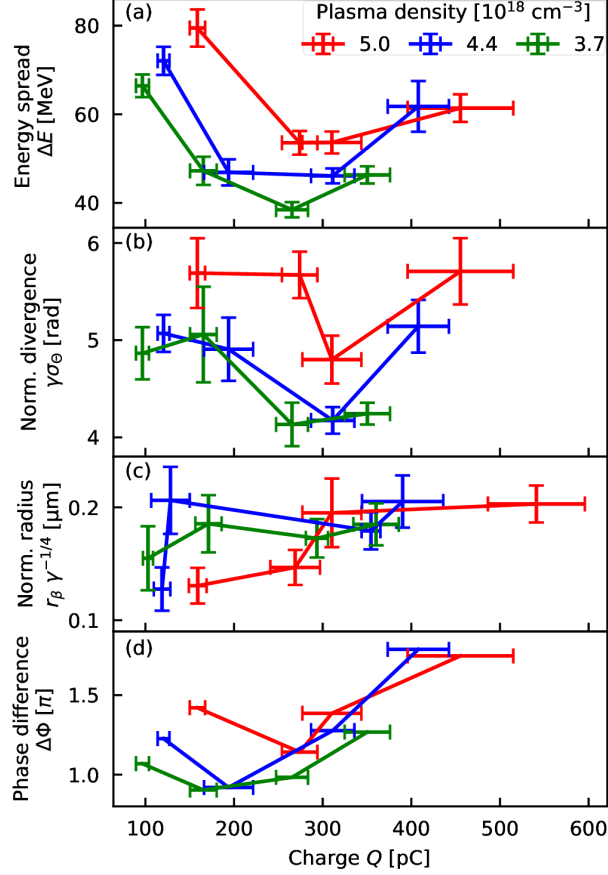


Figure 3. Measured energy spread (a), normalized divergence $\gamma\sigma_\theta$ (b), betatron radius $r_\beta\gamma^{-1/4}$ (c) and calculated betatron phase difference $\Delta\phi$ according to Eq. (1) (d) obtained from electron bunches with different charges and at three different plasma densities. Every data point represents the average of up to 15 shots with constant experimental parameters.

profile.

The data sets presented in this letter were taken during the same experimental campaign as those of Ref. [10] and follow a similar statistical significance of up to 15 consecutive shots. The amount of injected charge was tuned by varying the nitrogen concentration, keeping the laser parameters and plasma density constant. Due to the beam loading effect, the energy spread of the accelerated electron beams depends strongly on the injected charge, reaching a minimum value at around 300 pC, as shown in Fig. 3(a). The same trend holds for the energy (see supplementary information [44]).

In order to investigate the effect of beam loading on the transverse electron dynamics, the geometric divergence of the bunch σ_θ was extracted from the non-dispersive plane of the electron spectrometer after having left the plasma accelerator. Fig. 3(b) shows the normalized divergence $\gamma\sigma_\theta$ for various plasma

densities where γ is the relativistic Lorentz factor. At around 300 pC where the optimum beam loading occurs [10], a drop of up to 20 % of the normalized beam divergence is consistently observed for all plasma density sets. This suggests that accelerator geometry, i.e., cavity size, plasma wavelength and the plasma down-ramp length, does not play a dominant role in the observed effect.

Additionally, the betatron source size, thus the electron beam radius at the end of the accelerator, was deduced from the betatron spectrum by modeling synchrotron radiation [33, 36]. Errors caused by shot-to-shot fluctuation resulting in jitter of the betatron pointing were avoided by excluding off-center shots using the transverse betatron profile diagnostic. Only shots within one data set were selected where the betatron radiation cone was oriented on-axis. Fig. 3(c) presents the reconstructed betatron source radii $r_\beta \gamma^{-1/4}$. The $\gamma^{-1/4}$ factor normalizes differences in energy gain [2]. Note that the betatron radius expresses no extremum at 300 pC but indicates a constant micrometer-small source size at the plasma accelerator exit for different experimental parameters. For this spatially compact bunch, the normalized divergence shows a fairly similar value for the lowest and highest charges. Thus, space charge does not dominate the beam divergence as the bunch propagates in the drift space after acceleration. Otherwise, a monotonic increase of the beam divergence with charge should be visible.

Because space charge cannot explain the reduced beam divergence observed at matched beam loading, we focus on the influence of beam energy spread on beam decoherence. For optimum beam loading the relative beam energy spread reaches a minimum value. The length required for the full decoherence can be estimated by $l_{dc} = 2.35\lambda_\beta \langle E \rangle / \Delta E$ [26, 45]. Here, $\lambda_\beta = \sqrt{2\gamma}\lambda_p$ is the betatron wavelength, $\lambda_p = 2\pi c/\omega_p$ the plasma wavelength, c the speed of light in vacuum, ω_p the plasma frequency, ΔE the energy spread (FWHM), and $\langle E \rangle$ the average energy of the peaked spectrum. For the observed energy range, l_{dc} is always longer than two millimeters which is more than the acceleration length l_{acc} of 1.6 mm, indicated by simulation [44]. The short acceleration length suggests that the accelerated electron bunches have not fully experienced beam decoherence at the end of the plasma channel. Thus, the difference of the betatron phase between the highest and lowest energy electrons can quantify the degree of decoherence.

In transverse phase space (x, p_x) , electrons at given energy orbit at a different frequency compared to electrons at other energies [27]. A group i of electrons with the energy γ_i gains the betatron phase $\phi_i = \int_0^{l_{acc}} dt \omega_{\beta,i}$ over the acceleration length, with $\omega_{\beta,i} = 2\pi c/\lambda_{\beta,i}$ being the betatron frequency. With the maximum and minimum phase for $i = 1, 2$, full decoherence is equivalent to a phase difference $\Delta\phi = \phi_1 - \phi_2 \geq \pi$. Furthermore, the duration of the injection process determines the initial transverse phase space. Electrons injected earlier have already performed phase space rotation while other electrons are still being trapped. For the case of STII with an injection duration shorter than π/ω_p , beam size and transverse momentum spread can exhibit oscillations in (x, p_x) [27]. The phase difference $\Delta\phi$ is given by [27]:

$$\Delta\phi \approx \frac{\sqrt{2}}{E_{z,1}} \sqrt{E_{z,1} k_p l_{acc} + 1} - \frac{\sqrt{2}}{E_{z,2}} \sqrt{E_{z,2} k_p l_{acc} + 1}, \quad (1)$$

where $k_p = 2\pi/\lambda_p$ is the plasma wavenumber. The electric fields $E_{z,i}$ at the

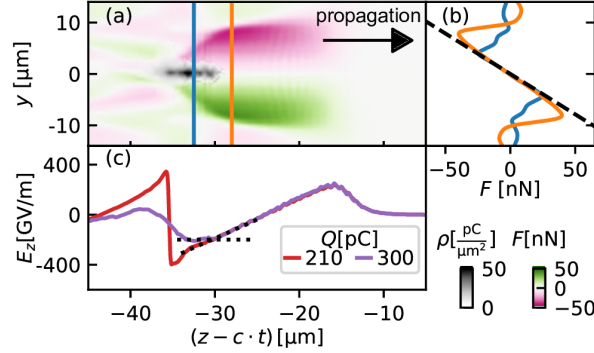


Figure 4. Matched beam loading in simulation: (a) illustrates the focusing force map with an injected charge of 300 pC at $z = 1.7$ mm. The density of trapped and accelerated electrons from the nitrogen’s K-shell and the focusing force are indicated by the gray and color scale at the bottom right, respectively. (b) presents two lineouts of the focusing force in front of the bunch (orange) and at the bunch (blue) emphasizing its linearity. The black dashed line in (b) indicates the theoretically predicted value [47]. (c) shows the accelerating fields for injected charges of 300 pC and 210 pC. The black dotted lines illustrate the local flattening of the acceleration field for matched beam loading close to 300 pC.

bunch’s head and tail are deduced from the measured maximum energy gain and energy spread and are normalized to $m_e \omega_p c / e$, where m_e and e are the electron rest mass and the charge, respectively. Fig. 3(d) presents the calculated phase difference according to Eq. (1). In general, the minimum $\Delta\phi$ is in good agreement with the expected optimum beam loading condition, appearing at slightly lower charges than the minimum of $\gamma\sigma_\theta$. This demonstrates that a low energy spread leads to the reduction of the beam decoherence resulting in electron beams of small divergence.

An upper limit for the normalized emittance of $\epsilon_n = \gamma\sigma_\theta r_b$ can be derived from the simultaneously recorded beam divergence and radius r_b . The latter can be deduced from r_β by $r_b = r_\beta / \sqrt{2}$ [46]. Typical values of the beam size are in the range of 0.56 μm to 0.7 μm at the accelerator exit. Together with $\gamma\sigma_\theta$ varying from 4 rad to 5.6 rad, the resulting normalized emittance reaches 2 mm mrad to 4 mm mrad which is comparable with typical values for LWFA when applying ionization injection [2, 9].

Parallel to the experimental work, three-dimensional particle-in-cell (PIC) simulations were performed with the PIconGPU code [48, 49] taking realistic experimental parameters [44]. With these simulations the influence of beam loading on the focusing fields and transverse phase space can be confirmed. Fig. 4(a) illustrates the focusing field map from two plasma cavities loaded with an injected charge of 300 pC. Note that the focusing force is extended to smaller $(z-ct)$ because of the large amount of injected charge, demonstrating the beam loading effect [29]. The blue and orange lineouts in Fig. 4(b) are sampling the focusing force at different longitudinal positions, i.e., in the front of the bunch and at the bunch center, respectively, emphasizing the linearity and independence of space charge. Fig. 4(c) illustrates the effect of beam loading on the

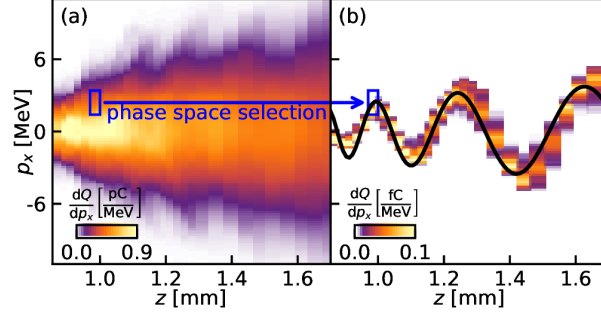


Figure 5. The transverse momentum p_x in simulation: (a) indicates an increase with weak modulations of the transverse momentum of the electrons during acceleration. (b) shows the betatron oscillation of a macro-particle subset. The black line shows the semi-analytic model from Ref. [30] assuming an adiabatic acceleration.

acceleration field. The weak loading of a small bunch charge (210 pC) maintains the typical linear field gradient. With strong beam loading (300 pC), the field becomes constant along the bunch, minimizing the energy spread accumulated during acceleration. Summarizing, beam loading does not directly couple the longitudinal and transverse fields of the plasma cavity.

Fig. 5 presents the temporal evolution of the transverse momentum for the bunch and a subset of ~ 4000 macro-particles. As shown in Fig. 5(a), the entire bunch experiences periodic modulations in p_x , indicating that the bunch has not reached full decoherence yet. This confirms the estimate of the decoherence length. The modulations can be attributed to the betatron oscillations as denoted for a macro-particles subset in Fig. 5(b). The subset contains macro-particles with same initial position and momentum. The black curve represents the theoretically predicted evolution in phase space according to [30] and agrees well with the simulated data.

In conclusion, we have shown that the experimental observation of the charge dependent minimum in normalized beam divergence can be explained by incomplete decoherence of the betatron oscillations in the bunch. The finding is an essential step towards the generation of electron bunches with small normalized divergence and energy spread at high peak current. Furthermore, tuning the energy spread can control the beam divergence via the betatron decoherence process. The next generation of high-flux light sources will benefit from less divergent electron sources and beam transport to a subsequent setup such as an insertion device will be facilitated.

The authors gratefully acknowledge the team from DRACO as well as T. Cowan, M. Downer, J. Grenzer A. Laso García, K. Steiniger, A. Wagner and R. Zgadzaj for their support. This work was partly supported by EuCARD-2, funding under Grand Agreement No. 312453, and by HZDR under programme Matter and Technology. The PIC simulations were performed at the Center for Information Services and High Performance Computing (ZIH) at TU Dresden.

References

1. E. Esarey, C. B. Schroeder, and W. P. Leemans, *Rev. Mod. Phys.* **81**, 1229 (2009).
2. M. C. Downer, R. Zgadzaj, A. Debus, U. Schramm, and M. C. Kaluza, *Rev. Mod. Phys.* **90**, 035002 (2018).
3. A. J. Gonsalves, K. Nakamura, J. Daniels, C. Benedetti, C. Pieronek, T. C. H. de Raadt, S. Steinke, J. H. Bin, S. S. Bulanov, J. van Tilborg, C. G. R. Geddes, C. B. Schroeder, C. Tóth, E. Esarey, K. Swanson, L. Fan-Chiang, G. Bagdasarov, N. Bobrova, V. Gasilov, G. Korn, P. Sasorov, and W. P. Leemans, *Phys. Rev. Lett.* **122**, 084801 (2019).
4. C. G. R. Geddes, K. Nakamura, G. Plateau, C. Toth, E. Cormier-Michel, E. Esarey, C. B. Schroeder, J. Cary, and W. P. Leemans, *Physical Review Letters* **100**, 1 (2008).
5. J. Osterhoff, A. Popp, Z. Major, B. Marx, T. P. Rowlands-Rees, M. Fuchs, M. Geissler, R. Hörlein, B. Hidding, S. Becker, E. A. Peralta, U. Schramm, F. Grüner, D. Habs, F. Krausz, S. M. Hooker, and S. Karsch, *Phys. Rev. Lett.* **101**, 085002 (2008).
6. C. Rechatin, J. Faure, A. Ben-Ismaïl, J. Lim, R. Fitour, A. Specka, H. Videau, A. Tafzi, F. Burgy, and V. Malka, *Phys. Rev. Lett.* **102**, 1 (2009).
7. A. J. Gonsalves, K. Nakamura, C. Lin, D. Panasenkov, S. Shiraishi, T. Sokollik, C. Benedetti, C. B. Schroeder, C. G. R. Geddes, J. van Tilborg, J. Osterhoff, E. Esarey, C. Toth, and W. P. Leemans, *Nat. Phys.* **7**, 862 (2011).
8. A. Buck, J. Wenz, J. Xu, K. Khrennikov, K. Schmid, M. Heigoldt, J. M. Mikhailova, M. Geissler, B. Shen, F. Krausz, S. Karsch, and L. Veisz, *Phys. Rev. Lett.* **110**, 185006 (2013).
9. A. Irman, J. P. Couperus, A. Debus, A. Köhler, J. M. Krämer, R. Pausch, O. Zarini, and U. Schramm, *Plasma Physics and Controlled Fusion* **60** (2018), 10.1088/1361-6587/aaef1.
10. J. P. Couperus, R. Pausch, A. Köhler, O. Zarini, J. M. Krämer, M. Garten, A. Huebl, R. Gebhardt, U. Helbig, S. Bock, K. Zeil, A. Debus, M. Bussmann, U. Schramm, and A. Irman, *Nature Communications* **8**, 487 (2017).
11. Y. Glinec, J. Faure, A. Norlin, A. Pukhov, and V. Malka, *Phys. Rev. Lett.* **98**, 194801 (2007).
12. A. D. Debus, M. Bussmann, U. Schramm, R. Sauerbrey, C. D. Murphy, Z. Major, R. Hörlein, L. Veisz, K. Schmid, J. Schreiber, K. Witte, S. P. Jamison, J. G. Gallacher, D. A. Jaroszynski, M. C. Kaluza, B. Hidding, S. Kiselev, R. Heathcote, P. S. Foster, D. Neely, E. J. Divall, C. J. Hooker, J. M. Smith, K. Ertel, A. J. Langley, P. Norreys, J. L. Collier, and S. Karsch, *Physical Review Letters* **104**, 1 (2010).

-
13. O. Lundh, J. Lim, C. Rechatin, L. Ammoura, A. Ben-Ismaïl, X. Davoine, G. Gallot, J.-P. Goddet, E. Lefebvre, V. Malka, and J. Faure, *Nature Physics* **7**, 219 (2011).
 14. O. Zarini, A. Köhler, J. Couperus, R. Pausch, T. Kurz, S. Schöbel, H. Meißner, M. Bussmann, U. Schramm, A. Irman, and A. Debus, in *IEEE Advanced Accelerator Concepts Workshop (AAC)* (IEEE, 2018) pp. 1–5, 978-1-5386-7721-6.
 15. B. Green, S. Kovalev, V. Asgekar, G. Geloni, U. Lehnert, T. Golz, M. Kuntzsch, C. Bauer, J. Hauser, J. Voigtlaender, B. Wustmann, I. Koesterke, M. Schwarz, M. Freitag, A. Arnold, J. Teichert, M. Justus, W. Seidel, C. Ilgner, N. Awari, D. Nicoletti, S. Kaiser, Y. Laplace, S. Rajasekaran, L. Zhang, S. Winnerl, H. Schneider, G. Schay, I. Lorincz, A. A. Rauscher, I. Radu, S. Maehrlein, T. H. Kim, J. S. Lee, T. Kampfrath, S. Wall, J. Heberle, A. Malnasi-Csizmadia, A. Steiger, A. S. Müller, M. Helm, U. Schramm, T. Cowan, P. Michel, A. Cavalleri, A. S. Fisher, N. Stojanovic, and M. Gensch, *Scientific Reports* **6**, 22256 (2016).
 16. J. B. Rosenzweig, B. Breizman, T. Katsouleas, and J. J. Su, *Physical Review A* **44** (1991), 10.1103/PhysRevA.44.R6189.
 17. B. Hidding, T. Königstein, J. Osterholz, S. Karsch, O. Willi, and G. Pretzler, *Physical Review Letters* **104**, 1 (2010).
 18. A. Martinez De La Ossa, J. Grebenyuk, T. Mehrling, L. Schaper, and J. Osterhoff, *Physical Review Letters* **111** (2013), 10.1103/PhysRevLett.111.245003, 1309.1900 .
 19. H.-P. Schlenvoigt, K. Haupt, A. Debus, F. Budde, O. Jäckel, S. Pfotenhauer, H. Schwoerer, E. Rohwer, J. G. Gallacher, E. Brunetti, R. P. Shanks, S. M. Wiggins, and D. A. Jaroszynski, *Nature Physics* **4**, 130 (2008).
 20. M. Fuchs, R. Weingartner, A. Popp, Z. Major, S. Becker, J. Osterhoff, I. Cortie, B. Zeitler, R. Hörlein, G. D. Tsakiris, U. Schramm, T. P. Rowlands-Rees, S. M. Hooker, D. Habs, F. Krausz, S. Karsch, and F. Grüner, *Nature Physics* **5**, 826 (2009).
 21. A. R. Maier, A. Meseck, S. Reiche, C. B. Schroeder, T. Seggebrock, and F. Grüner, *Phys. Rev. X* **2**, 031019 (2012).
 22. Z. Huang, Y. Ding, and C. B. Schroeder, *Phys. Rev. Lett.* **109**, 204801 (2012).
 23. K. Steiniger, M. Bussmann, R. Pausch, T. Cowan, A. Irman, A. Jochmann, R. Sauerbrey, U. Schramm, and A. Debus, *Journal of Physics B: Atomic, Molecular and Optical Physics* **47**, 234011 (2014).
 24. T. Eichner, F. Grüner, S. Becker, M. Fuchs, D. Habs, R. Weingartner, U. Schramm, H. Backe, P. Kunz, and W. Lauth, *Phys. Rev. ST Accel. Beams* **10**, 082401 (2007).
-

-
25. T. André, I. A. Andriyash, A. Loulergue, M. Labat, E. Roussel, A. Ghaith, M. Khojoyan, C. Thaury, M. Valléau, F. Briquez, F. Marteau, K. Tavakoli, P. N'Gotta, Y. Dietrich, G. Lambert, V. Malka, C. Benabderahmane, J. Vétéran, L. Chapuis, T. El Ajjouri, M. Sebdaoui, N. Hubert, O. Marcouillé, P. Berteaud, N. Leclercq, M. El Ajjouri, P. Rommeluère, F. Bouvet, J. P. Duval, C. Kitegi, F. Blache, B. Mahieu, S. Corde, J. Gautier, K. Ta Phuoc, J. P. Goddet, A. Lestrade, C. Herbeaux, C. Évain, C. Sz waj, S. Bielawski, A. Tafzi, P. Rousseau, S. Smartsev, F. Polack, D. Dennetière, C. Bourassin-Bouchet, C. De Oliveira, and M.-E. Couprie, *Nature Communications* **9**, 1334 (2018).
 26. T. Mehrling, J. Grebenyuk, F. S. Tsung, K. Floettmann, and J. Osterhoff, *Physical Review Special Topics - Accelerators and Beams* **15**, 1 (2012).
 27. X. L. Xu, J. F. Hua, F. Li, C. J. Zhang, L. X. Yan, Y. C. Du, W. H. Huang, H. B. Chen, C. X. Tang, W. Lu, P. Yu, W. An, C. Joshi, and W. B. Mori, *Physical Review Letters* **112**, 1 (2014).
 28. T. Katsouleas, S. Wilks, J. M. Dawson, P. Chen, and J. J. Su, *Particle Accelerators* **22**, 210 (1987).
 29. M. Tzoufras, W. Lu, F. S. Tsung, C. Huang, W. B. Mori, T. Katsouleas, J. Vieira, R. A. Fonseca, and L. O. Silva, *Physical Review Letters* **101**, 1 (2008), 0809.0227 .
 30. A. G. Khachatryan, A. Irman, F. A. Van Goor, and K. J. Boller, *Physical Review Special Topics - Accelerators and Beams* **10**, 1 (2007).
 31. E. Esarey, B. Shadwick, P. Catravas, and W. Leemans, *Phys. Rev. E* **65**, 056505 (2002).
 32. F. Albert, R. Shah, K. T. Phuoc, R. Fitour, F. Burgy, J.-P. Rousseau, A. Tafzi, D. Douillet, T. Lefrou, and A. Rousse, *Phys. Rev. E* **77**, 056402 (2008).
 33. M. Schnell, A. Sävert, B. Landgraf, M. Reuter, M. Nicolai, O. Jäckel, C. Peth, T. Thiele, O. Jansen, A. Pukhov, O. Willi, M. C. Kaluza, and C. Spielmann, *Phys. Rev. Lett.* **108**, 1 (2012).
 34. S. Corde, K. Ta Phuoc, G. Lambert, R. Fitour, V. Malka, A. Rousse, A. Beck, and E. Lefebvre, *Reviews of Modern Physics* **85**, 1 (2013).
 35. G. R. Plateau, C. G. R. Geddes, D. B. Thorn, M. Chen, C. Benedetti, E. Esarey, A. J. Gonsalves, N. H. Matlis, K. Nakamura, C. B. Schroeder, S. Shiraishi, T. Sokollik, J. van Tilborg, C. Toth, S. Trotsenko, T. S. Kim, M. Battaglia, T. Stöhlker, and W. P. Leemans, *Phys. Rev. Lett.* **109**, 064802 (2012).
 36. A. Köhler, J. P. Couperus, O. Zarini, A. Jochmann, A. Irman, and U. Schramm, *Nuclear Instruments and Methods in Physics Research, Section A: Accelerators, Spectrometers, Detectors and Associated Equipment* **829**, 265 (2016).
-

-
37. U. Schramm, M. Bussmann, A. Irman, M. Siebold, K. Zeil, D. Albach, C. Bernert, S. Bock, F. Brack, J. Branco, J. Couperus, T. Cowan, A. Debus, C. Eisenmann, M. Garten, R. Gebhardt, S. Grams, U. Helbig, A. Huebl, T. Kluge, A. Köhler, J. Krämer, S. Kraft, F. Kroll, M. Kuntzsch, U. Lehnert, M. Loeser, J. Metzkes, P. Michel, L. Obst, R. Pausch, M. Rehwald, R. Sauerbrey, H. Schlenvoigt, K. Steiniger, and O. Zarini, *Journal of Physics: Conference Series* **874**, 012028 (2017).
 38. J. P. Couperus, A. Köhler, T. A. W. Wolterink, A. Jochmann, O. Zarini, H. M. J. Bastiaens, K. J. Boller, A. Irman, and U. Schramm, *Nuclear Instruments and Methods in Physics Research, Section A: Accelerators, Spectrometers, Detectors and Associated Equipment* **830**, 504 (2015).
 39. M. Zeng, M. Chen, Z. M. Sheng, W. B. Mori, and J. Zhang, *Physics of Plasmas* **21** (2014), 10.1063/1.4868404, 1312.5825 .
 40. M. Mirzaie, S. Li, M. Zeng, N. A. M. Hafz, M. Chen, G. Y. Li, and Q. J. Zhu, *Scientific reports* , 1 (2015).
 41. T. Kurz, J. P. Couperus, J. M. Krämer, H. Ding, S. Kuschel, A. Köhler, O. Zarini, D. Hollatz, D. Schinkel, R. D’Arcy, J.-P. Schwinkendorf, J. Osterhoff, A. Irman, U. Schramm, and S. Karsch, *Review of Scientific Instruments* **89**, 093303 (2018).
 42. A. Jochmann, A. Irman, M. Bussmann, J. P. Couperus, T. E. Cowan, A. D. Debus, M. Kuntzsch, K. W. D. Ledingham, U. Lehnert, R. Sauerbrey, H. P. Schlenvoigt, D. Seipt, T. Stöhlker, D. B. Thorn, S. Trotsenko, A. Wagner, and U. Schramm, *Phys. Rev. Lett.* **111**, 114803 (2013).
 43. J. M. Krämer, A. Jochmann, M. Budde, M. Bussmann, J. P. Couperus, T. E. Cowan, A. Debus, A. Köhler, M. Kuntzsch, A. Laso García, U. Lehnert, P. Michel, R. Pausch, O. Zarini, U. Schramm, and A. Irman, *Scientific Reports* **8**, 1398 (2018).
 44. “See supplemental material at [url will be inserted by publisher].” .
 45. P. Michel, C. B. Schroeder, B. A. Shadwick, E. Esarey, and W. P. Lee-mans, *Physical Review E - Statistical, Nonlinear, and Soft Matter Physics* **74**, 1 (2006).
 46. A. Curcio, M. Anania, F. Bisesto, E. Chiadroni, A. Cianchi, M. Ferrario, F. Filippi, D. Giulietti, A. Marocchino, M. Petrarca, V. Shpakov, and A. Zigler, *Physical Review Accelerators and Beams* **20**, 012801 (2017).
 47. W. Lu, M. Tzoufras, C. Joshi, F. S. Tsung, W. B. Mori, J. Vieira, R. A. Fonseca, and L. O. Silva, *Phys. Rev. Spec. Top. - Accel. Beams* **10**, 1 (2007), 0612227 [physics] .
 48. H. Burau, R. Widera, W. Honig, G. Juckeland, A. Debus, T. Kluge, U. Schramm, T. E. Cowan, R. Sauerbrey, and M. Bussmann, *IEEE Transactions on Plasma Science* **38**, 2831 (2010).
 49. A. Huebl, R. Widera, B. Worpitz, R. Pausch, H. Burau, M. Garten, S. Starke, A. Grund, A. Debus, A. Matthes, S. Bastrakov, K. Steiniger, I. Göthel, S. Rudat, J. Kelling, and M. Bussmann, (2018), 10.5281/ZEN-ODO.1478937.
-

Minimizing betatron coupling of energy spread and divergence in laser-wakefield accelerated electron beams

A. Koehler^{1,2,*}, R. Pausch¹, J.P. Couperus Cabadağ¹, O. Zarini^{1,2},
J.M. Krämer¹, M. Bussmann¹, A. Debus¹, U. Schramm^{1,2}, A. Irman¹

1 Helmholtz-Zentrum Dresden - Rossendorf, Bautzner Landstrasse
400, 01328 Dresden, Germany

2 Technische Universität Dresden, 01062 Dresden, Germany

* a.koehler@hzdr.de

Additional experimental plots

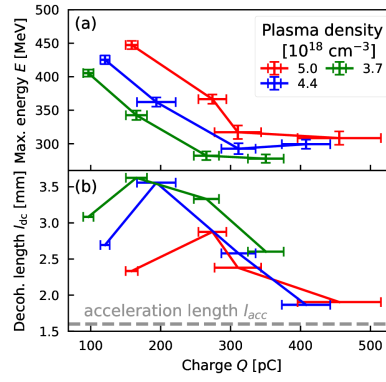


Figure 1. (a) shows the maximum attained energy E and (b) presents the betatron decoherence length $l_{dc} = 2.35\lambda_\beta\langle E\rangle/\Delta E$ for the data shown in the Letter.

PIC simulations

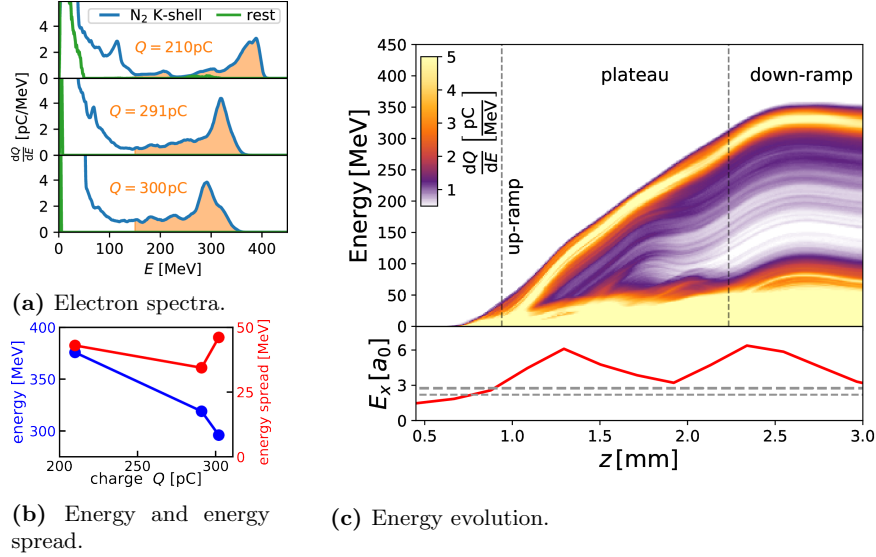


Figure 2. Overview of PIC simulations: (a) shows the electron energy histograms of three simulations with 1 %, 3 % and 5 % nitrogen doping. (b) illustrates the charge dependency of energy and energy spread of the simulations shown in (a). The top plot in (c) illustrates the electron energy evolution during the acceleration. The bottom plot in (c) illustrates the on-axis laser strength. The gray dashed lines indicate the required field strength for ionization of the first and second K-shell electron of nitrogen.

The PIC simulations utilized a laser pulse that was modeled using a Gaussian-Laguerre envelope in space and a Gaussian envelope in time. The laser wavelength was $\lambda_0 = 800$ nm and a pulse length was 30 fs (full-width at half-maximum). The simulation box consisted of $768 \times 768 \times 2016$ cells and had a transverse resolution of $0.33\lambda_0$, a longitudinal resolution of $0.05\lambda_0$ and a temporal resolution of $0.05c/\lambda_0$, where c is the speed of light. Such spatio-temporal resolution is required in order to numerically investigate the dynamics of the wakefield and plasma electrons. All simulations were performed with particle identifiers that allowed particle tracking of the nitrogen K-shell electrons.